Applicability of Euler Analysis to Prop-Fan Aerodynamic Design

by
Makoto Kobayakawa and Ryoji Takaki
Kyoto University, Kyoto 606, Japan
Yoshifumi Kawakami
Sumitomo Precision Products Ltd., Amagasaki 660, Japan
and
Frederick B. Metzger
Hamilton Standard, United Technologies Corporation
Windsor Locks, Connecticut 06096, USA

Abstract

Applicability of a numerical code to aerodynamic design of a Prop-Fan is guaranteed by precise agreement of numerical results with experimental data, i.e. not only integrated performance indices, such as power coefficient, net efficiency but also pressure distribution on the blade surface should agree well between computed and experimental results. In order for this purpose, an Euler Code using the TVD scheme is developed. The numerical calculations are performed for the SR-7L Prop-Fan at the freestream Mach number 0.5. The computed power coefficient, $C_P = 1.734$ shows comparatively good agreement with the experimental data, $C_P = 1.440 \pm 0.080$ if the measurement error of the blade twisted angle is considered and, furthermore, the computed pressure distributions on the blade surfaces show also good agreement.

1. Introduction

During thirteen years since the Prop-Fan technology projects started as a new conceptual propulsion system. Many experimental investigations, such as wind tunnel tests and FTB (Flying Test Bed), have been performed mainly in USA, and the results were applied effectively to the real Prop-Fan design. However, there remain many problems still which must be resolved.

At the same time, in the last decade we have seen so fast progress of the computational aerodynamics and many papers about Prop-Fan aerodynamics through computations were published. The authors also presented several kinds of computational results by VLM(Vortex Lattice Method)[1], potential analysis[2], Euler and Navier-Stokes analyses[2], [3] for the Prop-Fan models. However, it is necessary now to examine the applicability of the numerical computation to the aerodynamic design of real Prop-Fan. Especially, not only integrated performance indices, such as efficiency and power coefficient, but more precise phenomena on the blade, such as pressure distribution and location of shock wave, should be compared with each other. In other words, applicability of a numerical code to aerodynamic design is guaranteed by precise agreement of the numerical results with experimental data for both cruising and takeoff conditions. Such a successful code seems to enable us to make a design chart only by numerical calculations without wind tunnel testing.

Recently, the experimental results of SR-7L Prop-Fan were published on the AIAA paper[4]. This paper confirms whether the Euler Code by the authors is effectively applied to the design of the real Prop-Fan. The objective of this paper is to make an Euler Code which yields satisfactory results for Prop-Fan design. In order for this purpose, we employed the TVD(Total Variation Diminishing) scheme together with the ADI(Alternating Direction Implicit) algorithm.

This code was used to calculate the flow around the SR-7L Prop-Fan and for comparison with wind tunnel test results.

Nomenclature

b	Blade chord
c	Speed of sound
C_{LD}	Design Lift Coefficient at each radial direction
C_P	Power coefficient
c_p	Pressure coefficient
D	Diameter of the Prop-Fan
e	Energy of unit volume
E, F, G, H	Flux vectors
h	Maximum thickness of an airfoil
J	Transformation Jacobian
K	Adjusting constant (Eq.(9))
p	Pressure
p_c	Corrected blade surface pressure
p_o	Tunnel static pressure
Q	Vector of conserved quantities
r	Section Radius
R	Tip radius
R_1, R_2	Riemann invariants
S	Entropy
u, v, w	Cylindrical velocity components
U, V, W	Contravariant velocity components
V_o	Tunnel velocity
V_t	Tangential velocity at pressure tap radius
X, Y, Z	Radial, transverse, and axial distances
$\bar{X}, \bar{Y}, \bar{Z}$	Coordinates of conformal mapping
z, r, ϕ	Cylindrical coordinates
γ	Ratio of specific heats
$\Delta\theta$	Blade twist angle at $0.75r/R$
Λ	Sweep angle at 50% chord
ξ, η, ζ	Coordinates of conformal mapping
ρ	Air density

ψ Cone angle
Ω Angular velocity of rotation

superscript and subscript
i,j,k Grid point
n Time level
∞ Freestream

2. Euler Equations

In the same way as other papers, non-orthogonal coordinate transformations of the governing equations are employed. It maps the surface of the nacelle and both sides of the blade onto constant coordinate surfaces. The basic orthogonal coordinate system is cylindrical with z oriented along the rotational axis, r extending radially outward from the z-axis, and ϕ the meridional angle measured from a vertical plane. This is illustrated in Fig.1. The cylindrical coordinate system is easier to apply for the rotating blade boundary conditions than the cartesian coordinate system.

Under the assumption of inviscid compressible flow, the governing partial differential equation in the weak conservation law form is given by

$$Q_t + E_\xi + F_\eta + G_\zeta + H = 0, \tag{1}$$

where

$$Q = \frac{1}{J}\begin{bmatrix}\rho\\ \rho u\\ \rho v\\ \rho w\\ e\end{bmatrix}, E = \frac{1}{J}\begin{bmatrix}\rho U\\ \rho uU + p\xi_z\\ \rho vU + p\xi_r\\ \rho wU + p\xi_\phi/r\\ (e+p)U - p\xi_t\end{bmatrix}, F = \frac{1}{J}\begin{bmatrix}\rho V\\ \rho uV + p\eta_z\\ \rho vV + p\eta_r\\ \rho wV + p\eta_\phi/r\\ (e+p)V - p\eta_t\end{bmatrix},$$

$$G = \frac{1}{J}\begin{bmatrix}\rho W\\ \rho uW + p\zeta_z\\ \rho vW + p\zeta_r\\ \rho wW + p\zeta_\phi/r\\ (e+p)W - p\zeta_t\end{bmatrix}, H = \frac{1}{Jr}\begin{bmatrix}\rho v\\ \rho uv\\ \rho(v^2-w^2)\\ 2\rho vw\\ (e+p)V\end{bmatrix},$$

$$e = \frac{p}{\gamma-1} + \frac{\rho}{2}(u^2+v^2+w^2).$$

In the above equations, H contains centrifugal and Coriolis force terms due to the blade rotation. U, V, and W are contravariant velocity components, and J is the transformation Jacobian. The unknown variables, pressure p, density ρ, cylindrical velocity components u, v, and w are nondimensionalized by p_∞, ρ_∞, and $c_\infty/\sqrt{\gamma}$, respectively, where c_∞ is the free-stream speed of sound and γ is the ratio of specific heats. Other quantities, time t and angular velocity Ω are nondimensionalized by $c_\infty/(D\sqrt{\gamma})$ and $D\sqrt{\gamma}/c_\infty$, respectively. Precise expressions for U, V, W, J and metrics are found in Refs.[5] and [6].

3. Numerical Method

The numerical algorithm used to solve the Euler equations in computational space is the noniterative, ADI schemes. The implicit procedure enhances the speed of convergence.

The Euler equations, Eq.(1) is changed into the following form using AF(Approximate Factorization) method.

$$\left[I - \lambda^\xi I^-_{i+\frac{1}{2}jk}\Delta_{i+\frac{1}{2}jk} + \lambda^\xi I^+_{i-\frac{1}{2}jk}\Delta_{i-\frac{1}{2}jk}\right]\left[I - \lambda^\eta J^-_{ij+\frac{1}{2}k}\Delta_{ij+\frac{1}{2}k} + \lambda^\eta J^+_{ij-\frac{1}{2}k}\Delta_{ij-\frac{1}{2}k}\right]$$
$$\times\left[I - \lambda^\zeta K^-_{ijk+\frac{1}{2}}\Delta_{ijk+\frac{1}{2}} + \lambda^\zeta K^+_{ijk-\frac{1}{2}}\Delta_{ijk-\frac{1}{2}}\right]\Delta Q^n_{ijk} = -\lambda^\xi\left[\tilde{E}^n_{i+\frac{1}{2}jk} - \tilde{E}^n_{i-\frac{1}{2}jk}\right]$$
$$-\lambda^\eta\left[\tilde{F}^n_{ij+\frac{1}{2}k} - \tilde{F}^n_{ij-\frac{1}{2}k}\right] - \lambda^\zeta\left[\tilde{G}^n_{ijk+\frac{1}{2}} - \tilde{G}^n_{ijk-\frac{1}{2}}\right] - \Delta t H_{ijk} \tag{2}$$

The relations between Jacobian matrices in non-orthogonal coordinates and the cylindrical coordinates are described precisely in Ref. [5]. In the above equation, the TVD scheme[7] is employed. The detailed expression of these schemes will be given in the next section.

The solution of Eq.(2) is obtained by sequential inversion procedures. At first, the right-hand side term (explicit part) is calculated at each grid point. Each of the implicit operators represents block-tridiagonal matrix. After LU-decomposition for each operator sequential inversion processes are performed and $\Delta Q^n_{ijk} = Q^{n+1}_{ijk} - Q^n_{ijk}$ is obtained at the final stage. In this calculation, the steady state condition is required and then $\Delta Q^n_{ijk} \to 0$.

4. TVD Scheme[7]

Undesirable oscillations in the solution are suppressed and resolution is improved by the TVD scheme. In this case, Eq.(2), Harten's TVD scheme is used. The detailed expressions of the TVD scheme for the rotating blades are given in this section.

$\tilde{E}_{i+\frac{1}{2}jk}, \tilde{F}_{ij+\frac{1}{2}k}$, and $\tilde{G}_{ijk+\frac{1}{2}}$, are called the numerical fluxes, and, for example, $\tilde{E}_{i+\frac{1}{2}jk}$ is defined by

$$\tilde{E}_{i+\frac{1}{2}jk} = \frac{1}{2}\left[E_{ijk} + E_{i+1jk}\right] +$$
$$\frac{1}{2}\sum_{l=1}^{5}\left[\sigma^l_{i+\frac{1}{2}}(g^l_i + g^l_{i+1}) - \Psi(a^l_{i+\frac{1}{2}} + \nu^l_{i+\frac{1}{2}})\alpha^l_{i+\frac{1}{2}}\right]R^l_{i+\frac{1}{2}}, \tag{3}$$

where

$$g^l_i = S\cdot max\left[0, min(|\alpha^l_{i+\frac{1}{2}}|, S\cdot\alpha^l_{i-\frac{1}{2}})\right], \qquad S = sign(\alpha^l_{i+\frac{1}{2}}),$$

$$\nu^l_{i+\frac{1}{2}} = \delta^l_{i+\frac{1}{2}}\sigma^l_{i+\frac{1}{2}}\begin{cases}(g^l_{i+1} - g^l_i)/\alpha^l_{i+\frac{1}{2}}, & \alpha_{i+\frac{1}{2}} \neq 0,\\ 0, & \alpha_{i+\frac{1}{2}} = 0,\end{cases}$$

$$\alpha^l_{i+\frac{1}{2}} = (R^l_{i+\frac{1}{2}})^{-1}\Delta_{i+\frac{1}{2}}Q,$$

$$\sigma_{i+\frac{1}{2}} = \sigma(a^l_{i+\frac{1}{2}}),$$

and

$$\sigma(z) = \frac{1}{2}\Psi(z) = \begin{cases}\frac{1}{4}(z^2/\delta + \delta), & |z| < \delta,\\ \frac{1}{2}|z|, & |z| \geq \delta.\end{cases}$$

Here, $\Delta_{i+\frac{1}{2}}Q = Q_{i+1} - Q_i$, and $a^l_{i+\frac{1}{2}}$ and $R^l_{i+\frac{1}{2}}$ denote the lth eigenvalue and right eigenvector of Jacobian matrix, $\partial F(Q_{i+\frac{1}{2}}/\partial Q_{i+\frac{1}{2}}$, respectively. To calculate $a^l_{i+\frac{1}{2}}$ and $R^l_{i+\frac{1}{2}}$, we use Roe's averaging. For simplicity we omitted the indices j,k in the above definition, and $\tilde{F}_{ij+\frac{1}{2}k}$ and $\tilde{G}_{ijk+\frac{1}{2}}$ are defined in a similar manner.

5. Boundary Conditions

In order to obtain an accurate solution, the boundary conditions are carefully specified. The following boundary conditions should be imposed.

i. Conditions along the ξ-direction : inflow and outflow conditions.
ii. Conditions along the η-direction : impermeable condition on the nacelle and outer boundary condition.
iii. Conditions along the ζ-direction : impermeable condition on the blades (including blade tip and trailing edge), and periodic condition.

Brief descriptions for the above conditions are given below. Free-stream values are used at the outer and inflow boundaries. On the nacelle surface and on the blade surfaces, tangency should be satisfied. This is accomplished by specifying the appropriate contravariant velocities, V and W to zero, in the case of the nacelle surface and the blades surfaces, respectively. The cylindrical components of velocity, u,v, and w are obtained by solving

$$\begin{bmatrix} u \\ v \\ w \end{bmatrix} = \frac{1}{J} \begin{bmatrix} (\eta_r\zeta_\phi - \eta_\phi\zeta_r)/r & -(\xi_r\zeta_\phi - \xi_\phi\zeta_r)/r & (\xi_r\eta_\phi - \eta_r\xi_\phi)/r \\ -(\eta_z\zeta_\phi - \eta_\phi\zeta_z)/r & (\xi_z\zeta_\phi - \xi_\phi\zeta_z)/r & -(\xi_z\eta_\phi - \eta_z\xi_\phi)/r \\ (\eta_z\zeta_r - \eta_r\zeta_z) & -(\xi_z\zeta_r - \xi_r\zeta_z) & -(\xi_z\eta_r - \eta_z\xi_r) \end{bmatrix} \begin{bmatrix} U - \xi_t \\ V - \eta_t \\ W - \zeta_t \end{bmatrix}. \tag{4}$$

In order to solve this system, contravariant velocities V and W are approximated by the adjacent grid points of the solid boundaries. Along the intersection of nacelle and blade, both V and W are set to zero. The pressure and density on the solid surfaces are also approximated from the interior points. However, along the tip, leading edge and trailing edge of the blades, variables on the upper and lower surfaces are averaged.

For a subsonic outflow condition, the generalized Riemann invariants are used to determine the variables. The generalized Riemann invariants are given by

$$R_1 = U - \frac{2c}{\gamma - 1} \qquad \text{and} \qquad R_2 = U + \frac{2c}{\gamma - 1}. \tag{5}$$

Since R_1 and R_2 are associated with the two characteristic velocities $U+c$, and $U-c$, $U+2c/(\gamma-1)$, S, V, and W are determined from the free-stream values and $U - 2c/(\gamma-1)$ are linearly extrapolated from the interior, where $c = \sqrt{\gamma p/\rho}$, $S = ln(p/\rho^\gamma)$ and U, V and W in the free stream are calculated by

$$\begin{bmatrix} U_\infty \\ V_\infty \\ W_\infty \end{bmatrix} = \begin{bmatrix} \xi_t \\ \eta_t \\ \zeta_t \end{bmatrix} + \begin{bmatrix} \xi_z & \xi_r & \xi_\phi/r \\ \eta_z & \eta_r & \eta_\phi/r \\ \zeta_z & \zeta_r & \zeta_\phi/r \end{bmatrix} \begin{bmatrix} u_\infty \\ 0 \\ 0 \end{bmatrix}. \tag{6}$$

For a supersonic outflow condition, linearly extrapolated values from the interior are used.

The free-stream condition is specified previously to the start up of calculations.

6. Grid System

A computational grid for calculating the flowfield around the Prop-Fan is generated by using an algebraic method. Generally, the Prop-Fan has many identical blades which are distributed with equal angles around the rotating axis. When the flight direction is parallel to this axis, and the nacelle are axisymmetric, the flowfield around all blades are the same, i.e. the flowfield is circumferentially periodic. Consequently, the domain between two neighboring blades is usually employed for the calculations.

The basic blade geometry for the SR-7L Prop-Fan is shown in Figs.2 and 3. Fig.2 shows the thickness, t/b, blade planform or chord ratio, b/D, sectional design lift coefficient C_{LD}, twist angle $\Delta\theta$ and cone angle ψ as a function of fractional radius, r/R. The airfoils used at each radial location are also indicated in Fig.2. It can be seen that NACA Series 65 Circular Arc (CA) are used from the root of the blade at $r/R = 0.2$ to the $0.36r/R$ station. At locations between $0.563r/R$ and the tip of the blade, NACA Series 16 airfoils are used. In the region between $0.36r/R$ and $0.563r/R$, transition airfoils are used to blend the characteristics of the Circular Arc and Series 16 airfoils. Fig.3 defines the spatial location of the blade. This definition requires the X, Y and Z dimension and sweep angle as a function of fractional radius.

In order to generate a grid system around such a complicated configuration, the procedure consists of three steps. Step one is composed of dividing the domain into many axisymmetric parts. Step two consists of generating a two-dimensional H-type grid around the airfoil which is the cross sectional form of the blade. Step three consists of connecting the above two-dimensional grids radially and the generation of the three-dimensional grid system is completed.

To avoid a discontinuity of grid lines in the outer region of the blade, a hypothetical blade is formed. This hypothetical blade has zero thickness and constant chord length. In the calculation, the grid points of this hypothetical blade are treated as flow points.

The configurations of nacelle are determined by their radius distribution $r_H(x)$ along the axis of rotation. In order to avoid the singular point at the top of the spinner, a circular cylinder with small radius is extended to the inflow boundary. The following transformation is introduced.

$$r^* = r - [r_H(x) - R_H]\frac{R - r}{R - r_H(x)}, \qquad (r_H(x) \le r \le R), \tag{7}$$

where r_H is nacelle radius and R_H is its maximum value. After transformation the area between the nacelle and the blade tip is transformed into the regions between cylinders from r_H to R. The outer part of the blade tip is transformed identically, i.e.

$$r^* = r, \qquad (r > R) \tag{8}$$

The region of $r_H \leq r^* \leq R$ is divided into equidistant parts, and the region of $r^* \geq R$ is divided into exponentially extending parts. Consequently, several cylindrical surfaces are made. The intersections of the blade surfaces with these cylindrical surfaces can be obtained by interpolations of some sample points of the blade surface. These form airfoils on the developed cylindrical surfaces. Then, H-type periodical grids are generated. For this grid generation a conformal mapping is used for the leading edge of the airfoil. The mapping function is given by

$$\bar{Z} = i\zeta^{\frac{1}{2}} + K\zeta, \tag{9}$$

where K is adjusting constant and

$$\bar{Z} = \bar{X} + i\bar{Y}, \qquad \zeta = \xi + i\eta \tag{10}$$

In Eqs.(9), and (10) the origin of the coordinate axes occurs at the leading edge. This mapping function is effective for an airfoil with large leading edge curvature such as the case being considered in this paper(NACA 16 and NACA 65/CA series airfoil sections). Fig.4 shows the generated grids around the SR-7L.

7. Wind Tunnel Test Results

The data used for comparison with the Euler Code calculations was obtained on a specially instrumented blade of the SR-7 Prop-Fan which was designed for flight test on a modified Lockheed Jetstar in the NASA funded Large Scale Advanced Prop-Fan (LAP) test program.

In the geometry of the SR-7L, it should be noted that the thickness h/b shown in Fig.3 is only correct for the non-instrumented blades of the SR-7L Prop-Fan. For the instrumented blade a skin cladding 0.64mm (0.25 inch) thick was bonded to both surfaces of blade. Transition from the leading edge to the cladding was accomplished by a smooth blend.

Pressure taps were distributed at 13 radial stations on the instrumented blade on both the face and camber side as shown in Fig.5. It should be noted that the radial locations were oriented along the predicted streamlines for the design cruise condition. On the face side, 16 pressure taps were distributed across the chord at each radial station. On the pressure side 20 taps were distributed across the chord at each radial station except at radial stations 12 and 13 where only 19 and 18 taps, respectively, were installed, due to space limitations.

The pressure tap system consists of plastic skins with radial channels bonded to each side of the blades. Each of the radial channels are connected to a tube at the root of the blade which is led out to the blade shank. In operation the pressure taps at only one radial location are active. All of the other taps are sealed off with tape. Therefore, 13 runs at the same operating condition were required to obtain a complete blade surface pressure map for one test condition.

The pressure signals from each pressure tap on the blade were transmitted through a Scanivalve mounted on the nose of the Prop-Fan spinner shown in Fig.6. This system allowed transmission of the pressure signals on the rotating blade to the stationary field for monitoring and recording. The Scanivalve had the capacity to transmit 36 channels of information. In operation each tube leading from a radial channel on the instrumented blade was connected to one channel of the Scanivalve. On the stationary side the Scanivalve had one pressure transducer which monitored one channel at a time. Smooth air flow to the Prop-Fan was insured by mounting the Scanivalve in an aerodynamic housing and enclosing the unbilical attached to the nose of the Scanivalve in an airfoil shaped housing.

Tests were conducted in the S1-MA Large Wind Tunnel at the Modane-Avrieux Aerothermodynamic Test Center operated by the Office National D'Etudes et des Recherches Aerospatiales (ONERA) in France. The Prop-Fan was driven by Twin Turbomeca gas turbine engines driving a common gearbox. Due to power limitations of the drive engines, the SR-7L could be tested with only two of the eight blades normally installed. This allowed operation at power loadings per blade similar to those that would occur at takeoff and cruise conditions in an eight blade configuration.

Tests were conducted at the 13 operating conditions in Table 1. Condition 1 thru 4 represent static conditions (no tunnel power although the Prop-Fan induces some flow) with various levels of power. This series was designed to provide information on leading edge vortex flow. Conditions 5 and 6 represent takeoff conditions. Conditions 7 thru 9 were designed to bracket the design cruise power loading of the SR-7L. Conditions 10 thru 13 were designed to investigate transonic flow effects.

For this paper the data obtained at test condition 8 are used. It is the condition which most closely approximates the design cruise condition of the SR-7L. At this design condition viscous effects should be a minimum so Euler Code results have the potential for good agreement.

It is expected that Navier-Stokes Codes will be required to accurately calculate the off design conditions particularly takeoff where a strong leading edge vortex has been observed. Furhtermore, the SR-7L has been designed to deflect to the aerodynamically defined shape shown in Figs.2 and 3 at the design condition. At other conditions the deflections will be different so calculations using the geometry of Figs.2 and 3 may be in error.

Fig.7 shows the data from test condition 8. Pressure coefficient as a function of chord is shown for five radial stations on the blade. The equation for the pressure coefficient plotted in Fig.7 is as follows:

$$c_p = \frac{p_c - p_o}{0.5\rho(V_o^2 + V_t^2)} \tag{11}$$

where the symbols are as defined in the Nomenclature. It should be noted that p_c , the corrected pressure on the blade includes a correction for the centrifugal pumping through the tubes and channels between the Scanivalve and each pressure tap [3]. It can be seen in Fig.7 that the blade is operating well at this condition since the chordwise pressure distribution is fairly flat at each radial station. Some evidence of a leading edge vortex can be seen at radial stations 10 and 13 but this probably affects the performance very little.

8. Results and Discussions

For the numerical simulation the flowfield around the SR-7L Prop-Fan is calculated through the analysis described in 2 to 6. In this calculation the numerical results and the experimental data are compared with each other at the Test Condition No. 8. As described in 7, free stream Mach number is 0.5, advance ratio is 3.055, and blade twisted angle at three quarter of the blade tip radius is 54.95 degree.

The experiment was conducted by using 2 bladed Prop-Fan model, however, the calculation is performed for 8 blades. Table 1 shows that the power coefficient of the experiment is $C_P = 0.360 \pm 0.020$, but for the 8 bladed Prop-Fan, this value should be increased 4 times, i.e. $C_P = 1.440 \pm 0.080$.

Space for the computation is taken as follows: the inflow and outflow boundaries are located at 5 tip radii for upstream and downstream direction, respectively, and the outer boundary is 2.5 radius in the radial direction. A total of 101 points in the axial direction, 30 points in the radial direction, and 31 points between adjacent blades in the circumferential direction were used for the calculations. On the blade 61 points in the chordwise direction and 16 points in the spanwise direction were used.

The blade should be deformed due to centrifugal loads during operation in the experiment. In the calculation such deformation was considered in its geometry parameter distributions shown in Fig.2.

Pressure distributions on the blade at 4 stations (Radial Stations 1, 3, 5, and 10 in Fig.6) are compared between the calculated and experimental values in Fig.8. The lines of the calculated distribution are coincident with the pressure tap lines in the experiment. The computed power coefficient is, $C_P = 1.734$ while the experimental result is $C_P = 1.440 \pm 0.080$, and the computed net efficiency is 0.730. The computed power coefficient is relatively different from the experimental one, however, some measurement error might occur in the blade twisted angle 54.95 degree. Therefore, including this fact, this value shows a good agreement.

At the Radial Station 1 the computed pressure distribution is different from the experimental values. This is due to the cascade effect in the numerical calculation. The flow velocity is accelerated in the narrow pathway between the blades, while no such effect occurred for 2 bladed Prop-Fan. At the Radial Stations 3, 5, and 10 the computed pressure distributions agree with the experimental values approximately.

Isobars on the camber and face sides of the blade are shown in Fig.9. Steep change of the pressure is seen near the leading edge on the camber side. Since the flowfield is subsonic everywhere, consequently no shock is observed on both sides of the blade.

Vector plots of the flow velocities just after the trailing edge are depicted in Fig.10. Tip vortex from the blade is clearly seen in this figure.

By the present calculations it can be said that approximate agreement of the power coefficient and the pressure distributions on the blade between the calculation and the experiment shows the validity of the present Euler Code to the aerodynamic design of the Prop-Fan.

However, the comparison was done for only one Test Condition 8, therefore, the calculation must be performed for other Test Conditions and compared with each experiment. Particularly, for the higher Mach number Test Condition (Test Condition No. 12) the present Euler Code must be valid because the TVD scheme used in this analysis is excellent to capture shock wave accurately.

Furthermore, the numerical analysis to the aerodynamic design of the Prop-Fan must be accomplished by the Navier-Stokes analysis which can afford applicability to the takeoff conditions (Test Condition Nos. 2 and 6). However, it must be very difficult due to the lack of good turbulence model.

9. Concluding Remarks

In order to verify the applicability of the Euler Code to the Prop-Fan aerodynamic design, the flowfield around the 8 bladed SR-7L Prop-Fan at freestream Mach number 0.5 was calculated. The algorithm used in the present analysis was the TVD scheme which is excellent in shock capturing. Furthermore, an ADI algorithm was adopted together with the TVD scheme.

The calculated values were compared with the experimental data which were got by the wind tunnel tests in the S1-MA Large Wind Tunnel at the Modane-Avrieux Aerothermodynamic Test Center (ONERA) in France. The important point in the verification is agreement of both results not only in the integrated performance indices, such as power coefficient, net efficiency but also in the pressure distributions on the blade surfaces.

The computed power coefficient by the present analysis ($C_P = 1.734$) shows relatively good agreement with that by the experiment ($C_P = 1.440 \pm 0.080$) including the measurement error of the blade twisted angle. The computed pressure distributions on the blade surfaces also show good agreement with those of the experiment.

The validity of the present Euler Code to the aerodynamic design of the Prop-Fan is verified for this case, however, other Test Conditions, such as higher Mach number condition, takeoff condition, are expected to be compared with each other. In order for this purpose, an extension to Navier-Stokes Code from the Euler Code must be required for the latter case.

References

[1] M. Kobayakawa and H. Onuma, 'Propeller Aerodynamic Performance by Vortex Lattice Method', Journal of Aircraft, Vol.22, No.8, pp.649-654, 1985.

[2] M. Kobayakawa et al, 'Calculations of High Speed Propeller Performance Using Finite Difference Methods', Proceedings of 15th Congress of the ICAS', pp.1451-1460, 1986.

[3] M. Kobayakawa and I. Hatano, 'Flow Field Around a Propeller by Navier-Stokes Equation Analysis', AIAA Paper 88-3150, 1988.

[4] W. A. Campbell et al, 'A Report on High Speed Wind Tunnel Testing of the Large Scale Advanced Prop-Fan', AIAA Paper 88-2802, 1988.

[5] D. S. Chaussee and P. Kutler, 'User's Manual for Three-Dimensional Analysis of Propeller Flow Fields', NASA Contractor Report 167959, 1983.

[6] L. J. Bober et al, 'Prediction of High Speed Propeller Flow Fields Using a Three-Dimensional Euler Analysis', AIAA Paper 83-0188, 1983.
[7] H. C. Yee et al, 'Implicit Total Variation Diminishing (TVD) Schemes for Steady-State Calculations', Journal of Computational Physics, 57, pp.327-360, 1985.
[8] P. R. Bushnell, 'Measurement of the Steady Surface Pressure Distribution on the Single Rotation Large Scale Advanced Prop-Fan Blade at Mach Numbers from 0.03 to 0.78', NASA CR 182124, 1988.

Acknowledgement

The authors wish to acknowledge the many contributions made to the work reported in this paper. NASA Lewis is acknowledged for supporting the acquisition of the test data on the SR-7 and the reduction of the test data. The Hamilton Standard team who built the special instrumented blade and acquired and processed the data are also acknowledged. Without dedicated effort from all who were involved, there would be no data available for comparison with calculations.

Figures

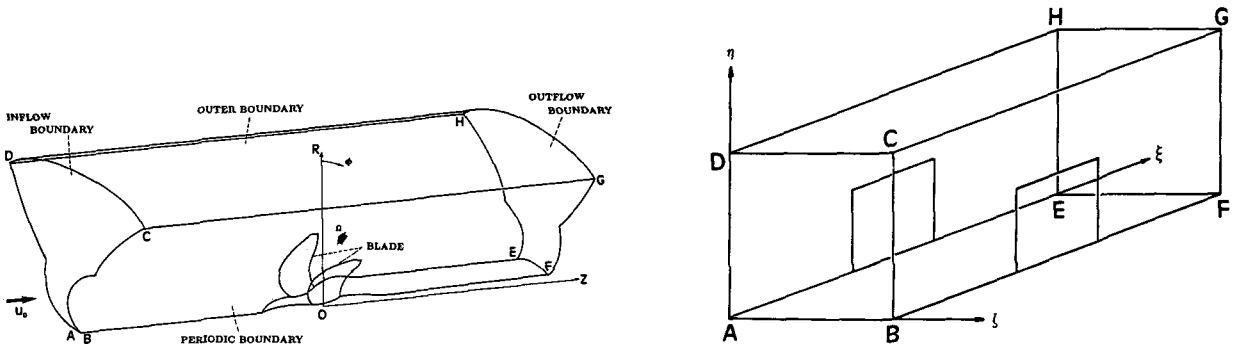

Fig.1 Physical space and computational space.

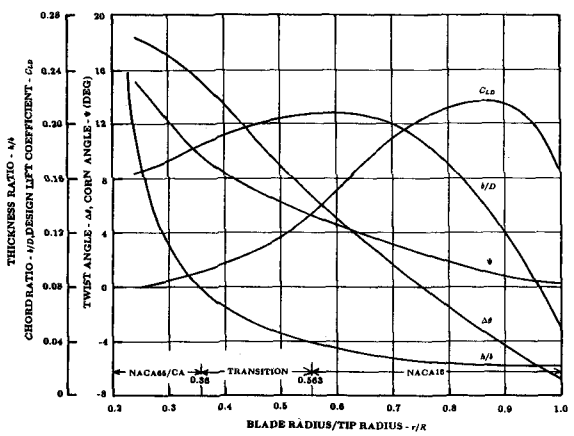

Fig.2 Basic blade geometry (1).

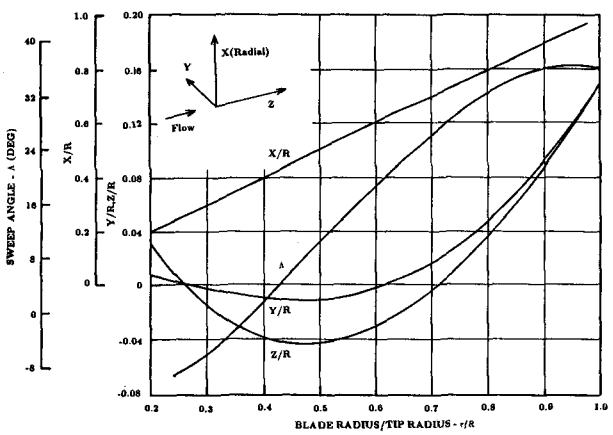

Fig.3 Basic blade geometry (2).

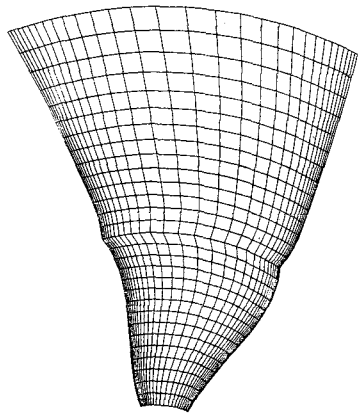

ξ-constant plane

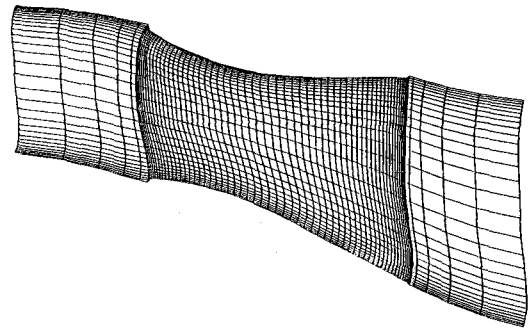

η-constant plane

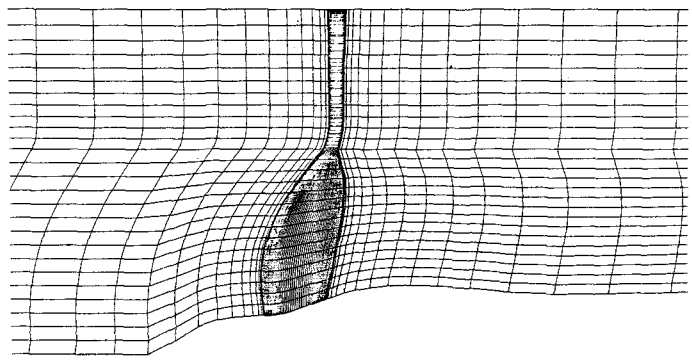

ζ-constant plane

Fig.4 Computational grids around SR-7L Prop-Fan.

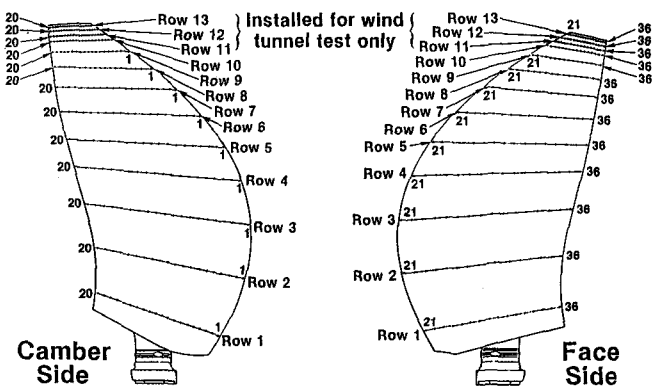

Fig.5 Distributions of pressure taps.

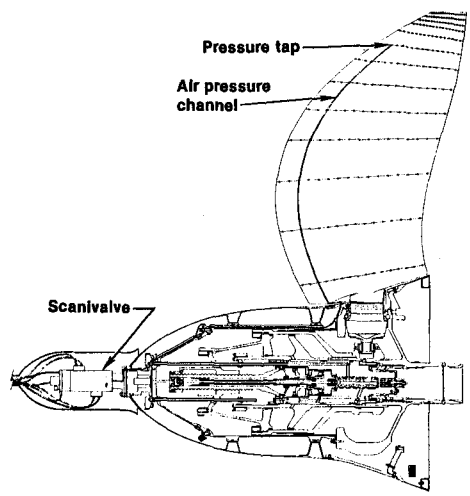

Fig.6 Scanivalve system.

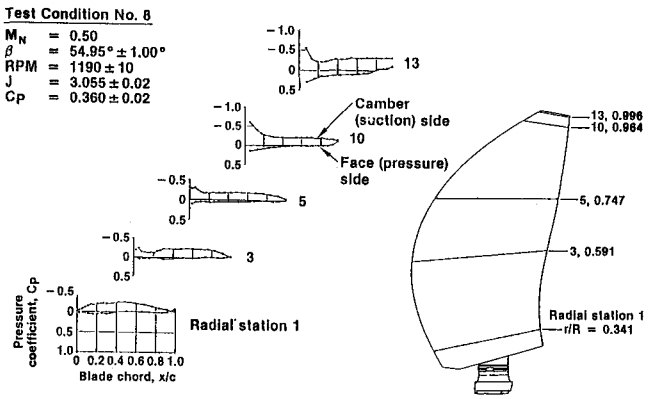

Fig.7 Pressure distribution of Test Condition 8.

Table 1 Wind tunnel test conditions.

Condition No.	M Mach No.	J Advance Ratio ±02	β Blade Angle ±1.00°	Cp Power Coefficient ±.02	N RPM ±10
1	.01	.08	13.80°	.079	1200
2	.02	.14	15.70°	.093	1200
3	.02	.15	18.78°	.152	1200
4	.03	.18	21.60°	.204	1200
5	.20	.88	25.65°	.098	1665
6	.20	.88	30.40°	.251	1651
7	.50	3.065	57.51°	.649	1186
8	.50	3.055	54.95°	.360	1190
9	.50	3.063	50.86°	.108	1185
10	.60	3.066	54.98°	.226	1436
11	.70	3.055	55.00°	.229	1685
12	.78	3.07	54.97°	.223	1840
13	.78	3.20	54.98°	.112	1782

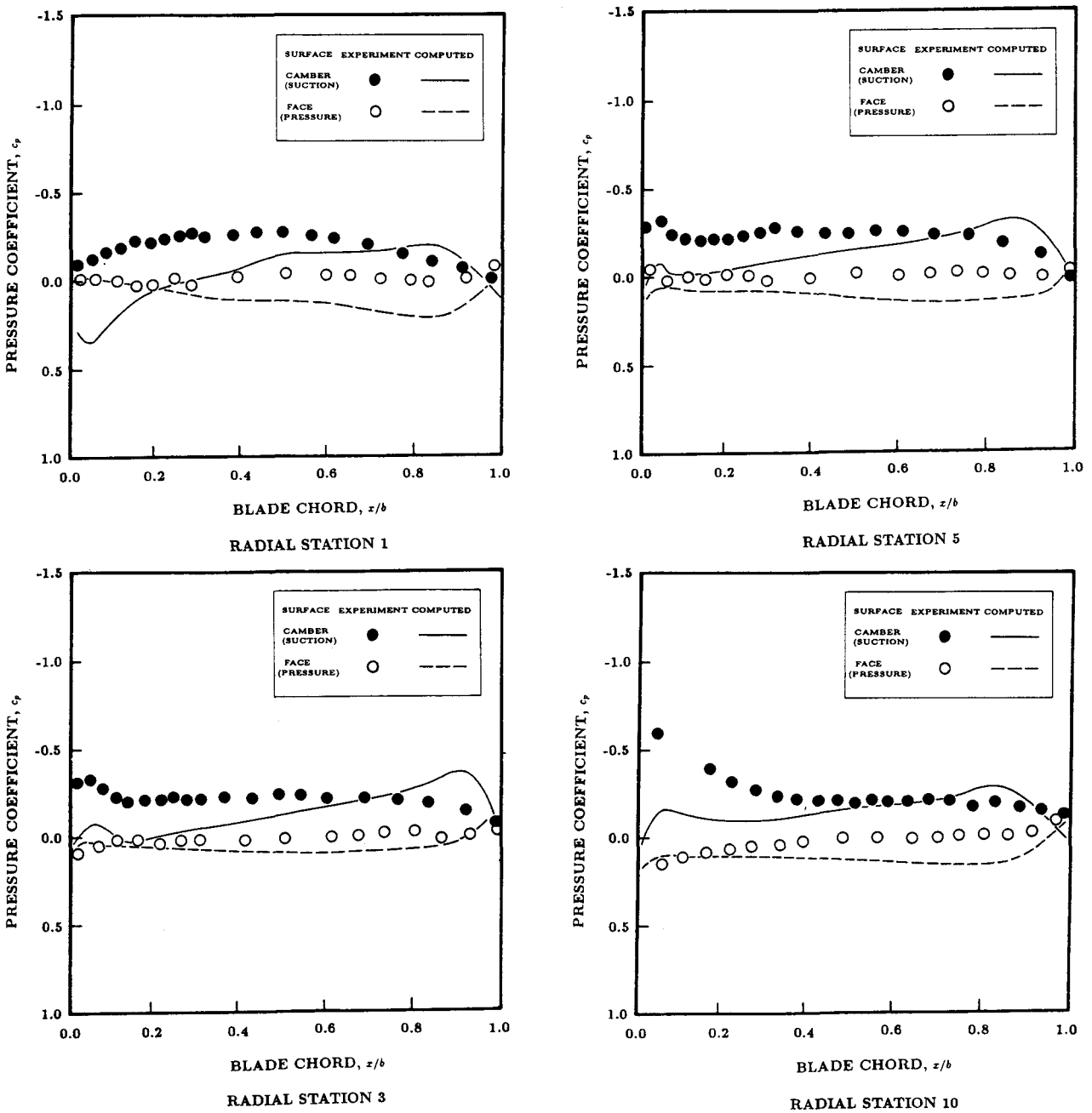

Fig.8 Comparison of pressure distributions.

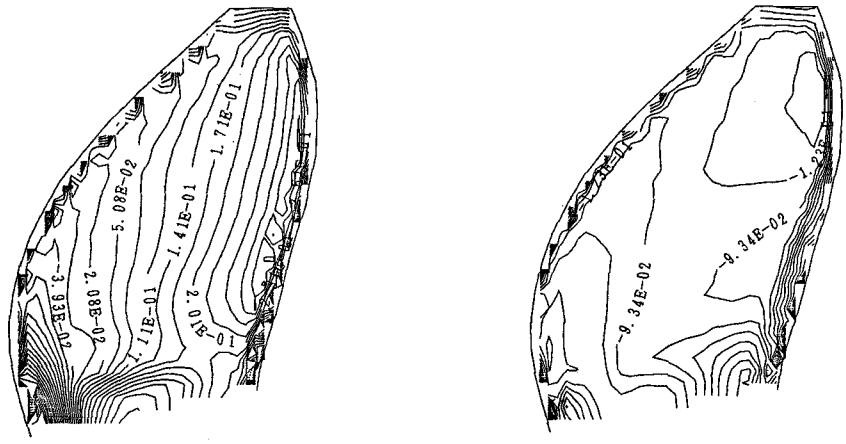

camber side face side

Fig.9 Isobars on blade surfaces.

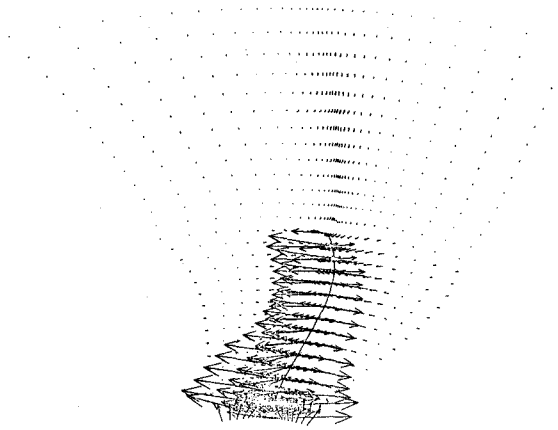

Fig.10 Vector plots of flow velocities.